ACS Sustainable Chemistry & Engineering

pubs.acs.org/journal/ascecg

Research Article

Mo_xC Heterostructures as Efficient Cocatalysts in Robust Mo_xC/g-C_3N_4 Nanocomposites for Photocatalytic H_2 Production from Ethanol

Yan Wang, Arturo Pajares, Jarosław Serafin, Xavier Alcobé, Frank Güell, Narcís Homs,* and Pilar Ramírez de la Piscina

Cite This: *ACS Sustainable Chem. Eng.* 2024, 12, 4365−4374

Read Online

ACCESS | Metrics & More | Article Recommendations | Supporting Information

ABSTRACT: In this work, we studied new materials free of noble metals that are active in photocatalytic H_2 generation from ethanol aqueous solutions ($EtOH_{aq}$), which can be obtained from biomass. Mo_xC/g-C_3N_4 photocatalysts containing hexagonal (hcp) Mo_2C and/or cubic (fcc) MoC nanoparticles on g-C_3N_4 nanosheets were prepared, characterized, and evaluated for photocatalytic hydrogen production from $EtOH_{aq}$ (25% v/v). Tailored Mo_xC/g-C_3N_4 nanocomposites with Mo_xC crystallite sizes in the 4−37 nm range were prepared by treatment with ultrasound of dispersions containing Mo_xC and g-C_3N_4 nanosheets, formerly synthesized. The characterization of the resulting nanocomposites, Mo_xC/g-C_3N_4, by different techniques, including photoelectrochemical measurements, allowed us to relate the photocatalytic performance of materials with the characteristics of the Mo_xC phase integrated onto g-C_3N_4. The samples containing smaller hcp Mo_2C crystallites showed better photocatalytic performance. The most performant nanocomposite contained nanoparticles of both hcp Mo_2C and fcc MoC and produced 27.9 mmol H_2 g^{-1} Mo; this sample showed the lowest recombination of photogenerated charges, the highest photocurrent response, and the lowest electron transfer resistance, which can be related to the presence of MoC-Mo_2C heterojunctions. Moreover, this material allows for easy reusability. This work provides new insights for future research on noble-metal-free g-C_3N_4-based photocatalysts.

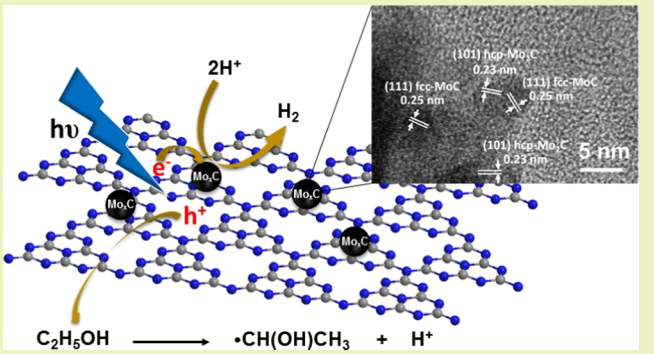

KEYWORDS: *molybdenum carbide, H_2 photoproduction, visible photocatalysis, Mo_xC cocatalyst, g-C_3N_4, bioethanol*

1. INTRODUCTION

Nowadays, the large-scale industrial production of H_2 is captive to fossil fuels. Thus, new ways to produce H_2 are of current interest in both the energy and environmental contexts. From this perspective, the development of photocatalytic systems that produce H_2 using renewable substrates, such as bioalcohols, is of primary importance.[1−4] Photocatalysts are usually based on inorganic semiconductor materials, and the direct use of solar radiation is highly attractive when the photocatalyst is able to absorb visible light. In this context, one of the most encouraging materials is graphitic carbon nitride (g-C_3N_4).[5−11] On the other hand, the main concern related to the efficiency of photocatalysts is the usually fast rate of recombination of the photogenerated charges, electrons (e^-), and holes (h^+).[12] Although the most common strategy that is used for improving h^+/e^- charge separation is the addition of noble metals to the surface of the semiconductor, other compounds such as transition metal oxides, sulfides, or carbides, have been also proposed as efficient cocatalysts.[13,14] Specifically, the catalytic properties of molybdenum and tungsten carbides are oftentimes described as Pt-like and they have been used as catalysts in different electrochemical and chemical processes and as cocatalysts in photochemical processes.[15−26] The use of molybdenum carbides in alternative hydrogen production, has been mainly focused on their use as electrocatalysts.[14] However, an increasing interest exists in the use of molybdenum carbide-based systems as cocatalysts in the photoproduction of H_2.[14] Different photocatalysts for H_2 evolution containing molybdenum carbides and semiconductors, such as TiO_2, CdS, and $SrTiO_3$, have been reported.[14,27−30] However, a limited number of papers dealing with photocatalysts based on Mo_2C and g-C_3N_4 have been published.[31−35] Mo−Mo_2C/g-C_3N_4 and Co-doped Mo−

Received: September 27, 2023
Revised: February 15, 2024
Accepted: February 15, 2024
Published: March 7, 2024

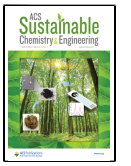

https://doi.org/10.1021/acssuschemeng.3c06261
ACS Sustainable Chem. Eng. 2024, 12, 4365−4374

Table 1. Several Characteristics of Photocatalysts[a]

sample	Mo content (wt %)	BET (m^2/g)	002 $g\text{-}C_3N_4$ (2θ deg)	crystallite size (nm)	band gap (eV)
$Mo_xC700/g\text{-}C_3N_4$	3.65	39	27.7	11 (Mo_2C)[b] 4 (MoC)[b]	2.79
$Mo_2C800/g\text{-}C_3N_4$	3.43	34	27.7	23 (Mo_2C)	2.79
$Mo_2C900/g\text{-}C_3N_4$	3.35	39	27.6	31 (Mo_2C)	2.78
$MoC1100/g\text{-}C_3N_4$	2.62	22	27.5	4 (MoC)	2.77
$Mo_2C\text{-comm}/g\text{-}C_3N_4$	3.33	22	27.5	37 (Mo_2C)	2.77
$g\text{-}C_3N_4$		31	27.7		2.75

[a]Mo content from chemical analysis (ICP-AES), BET surface area, position of the 002 XRD peak of $g\text{-}C_3N_4$, Mo_xC phase, crystallite size, and band gap values. [b]Calculated from the full profile analysis of the XRD pattern (Figure S6 [43]).

$Mo_2C/g\text{-}C_3N_4$,[31,35] $Mo_2C@C/g\text{-}C_3N_4$ heterostructures,[32,33] and rod-like $g\text{-}C_3N_4$ decorated with Mo_2C,[34] have been studied as photocatalysts in H_2 generation; in every case, triethanolamine (TEOA) solution was employed as sacrificial electron donor in the photocatalytic test. The presence of Mo, Co and Mo or C enhances the cocatalyst effect of Mo_2C onto $g\text{-}C_3N_4$.[31−35] On the other hand, it has been reported that the presence of MoC/Mo_2C heterostructures has a positive effect in the electrocatalytic behavior of molybdenum carbide-based catalysts for the H_2 evolution reaction.[36] Moreover, it has been proposed that, for a given material, there is a relationship between its performance in the electrocatalytic H_2 evolution and its efficiency as a cocatalyst in the photocatalytic H_2 production.[35]

This background and the advantage of using ethanol, which is currently produced and used as a biofuel around the world, led us to an in-depth study of photocatalysts based on $Mo_xC/g\text{-}C_3N_4$ (Mo_xC = Mo_2C and/or MoC) for H_2 production using $EtOH_{aq}$ and visible light. We have recently reported the preparation of molybdenum carbide phases via sol−gel methods using different molybdenum precursors and carbon sources; Mo_2C and/or MoC cubic and/or hexagonal were obtained depending on the preparation method used.[24,37−39] In this work, we report the preparation and characterization of new tailored $Mo_xC/g\text{-}C_3N_4$ photocatalysts, containing hcp Mo_2C and/or fcc MoC as cocatalysts with different crystallite sizes. Hydrogen production is related to the photoelectrochemical properties of the nanocomposites, which in turn depend on the crystalline phases of molybdenum carbide, including charge recombination, electron transfer resistance, and the photocurrent response of different photocatalysts.

2. EXPERIMENTAL SECTION

2.1. Synthesis of Mo_xC. Different Mo_xC phases were synthesized based on a recently described sol−gel method using $MoCl_5$ (reagent grade, 95%) and 4,5-dicyanoimidazole (DI) (reagent grade, 99%) from Sigma-Aldrich, as Mo and C sources, respectively.[37,38]

Specifically, the gel formed by the addition of $MoCl_5$ (5.6 mmol) and DI (2.8 mmol) to 15 mL of ethanol (>99.999% HPLC, Sigma-Aldrich), was treated at different temperatures under an Ar flow (99.999%, Linde) (T = 700, 800, or 900 °C) in a tubular furnace. The materials were labeled Mo_xCT, where T is the temperature used in the treatment. The preparation of Mo_xC1100 was accomplished using a similar method, with $MoCl_5$ (5.6 mmol), DI (5.6 mmol), and a thermal treatment of 1100 °C.

2.2. Preparation of $g\text{-}C_3N_4$ Nanosheets. For the preparation of $g\text{-}C_3N_4$ nanosheets, the thermal polymerization of melamine was accomplished as follows:[40] melamine (>99%, Alfa Aesar) was calcined at 5 °C/min up to 520 °C (4 h); the yellowish material was ground to powder, and the calcination process was repeated.

2.3. Integration of Mo_xCT onto $g\text{-}C_3N_4$. For the preparation of $Mo_xCT/g\text{-}C_3N_4$, dispersions in ethanol with the appropriate amounts of Mo_xCT and $g\text{-}C_3N_4$, to obtain about 3 wt% Mo, were treated under ultrasound (SONICS VCX 500) at 20 °C and 250 W for 1 h; then, ethanol was eliminated by careful evaporation with stirring at 50 °C. Moreover, using a similar procedure, commercial Alfa-Aesar Mo_2C (99.5% metal basis, hcp Mo_2C, average crystallite size $\overline{d}$ = 37 nm), was used for the preparation of the $Mo_2C\text{-comm}/g\text{-}C_3N_4$ photocatalyst. Table 1 lists all of the photocatalysts prepared and studied in this work.

2.4. Characterization of Photocatalysts. Inductively coupled plasma atomic emission spectrometry (ICP-AES) was used to determine the Mo content using a PerkinElmer Optima 3200RL instrument.

A Micromeritics Tristar II 3020 instrument was used to record the N_2 adsorption−desorption isotherms, which were determined at −196 °C after degasification at 250 °C under an Ar flow. Multipoint Brunauer−Emmett−Teller (BET) analysis of the isotherms was used to calculate the specific surface area (S_{BET}). The desorption isotherms were used for the determination of the pore size distribution by the method of Barrett−Joyner−Halenda (BJH).

Powder X-ray diffraction (XRD) patterns were recorded using a Bragg−Brentano powder diffractometer (PANalytical X'Pert PRO MPD), with Cu Kα radiation (λ = 1.5418 Å) from 2θ = 4 to 100°. Peak indexation and phase identification were performed with the aid of the ICDD Powder Diffraction File (PDF).[41] Accurate peak positions, area intensities, and full width at half-maximum (fwhm) were obtained after full profile analysis. The crystallite sizes were calculated from the fwhm using the Scherrer equation.[42] Semi-quantitative phase analysis, in some binary nanocrystalline samples, was performed from the accurate area intensities and using the reference intensity ratios in the corresponding PDF file.[43]

Fourier-transform infrared spectroscopy (FTIR) analysis was conducted by using pellets of the KBr-diluted samples on a Thermo Nicolet 5700 FTIR apparatus.

Transmission and high-resolution electron microscopy (TEM-HRTEM) and energy-dispersive X-ray (EDX) spectroscopy with elemental mapping analysis were performed using a JEOL JEM-2100 instrument operating at 200 kV.

X-ray photoelectron spectroscopy (XPS) was conducted using a PerkinElmer PHI-5500 Multitechnique System with Al Kα radiation (1486.6 eV). The binding energy (BE) values were determined using the C 1s peak at 284.8 eV, which was previously ascertained using Au as a reference. MultiPak XPS software was used to deconvolute the XPS signals.

UV−vis diffuse reflectance spectra (UV−vis DRS) were acquired using a PerkinElmer Lambda 950 UV/vis Spectrometer; $BaSO_4$ was used as a reference. The Kubelka−Munk model was used to determine the band gap values.

Photoluminescence (PL) spectroscopy measurements were performed at room temperature by using a Kimmon IK Series He−Cd CW laser (325 nm, 40 mW). Fluorescence was dispersed through a SpectraPro 2750 (focal length of 750 mm) f/9.8 monochromator, detected with a Hamamatsu H8259-02 photomultiplier, and amplified

https://doi.org/10.1021/acssuschemeng.3c06261
ACS Sustainable Chem. Eng. 2024, 12, 4365−4374

using a Stanford Research System SR830 DSP Lock-in amplifier. A 360 nm filter was used for the stray light, and the emission spectra were corrected using the optical transfer function of the PL setup.

For photoelectrochemical characterization of samples, electrochemical impedance spectroscopy (EIS) and transient photocurrent determination were performed. The system consisted of a computer-controlled potentiostat (VMP3, BioLogic Science Instruments) with an undivided three-electrode cell; a Pt wire was used as the counter electrode, Ag/AgCl (3 M KCl) as the reference, the photocatalyst (1 cm^2 geometric area) as the working electrode; and an aqueous solution of Na_2SO_4 (0.5 M) as the electrolyte. A150 W AM 1.5G solar simulator (Solar Light Co., 16S-300-002 v 4.0) with an incident light intensity of 1 sun (100 mW cm^{-2}) was used to perform the measurements under illumination.

2.5. Photocatalytic Experiments. Figure S1 shows a schematic diagram of the system used for the photocatalytic tests. It contained a jacketed reactor of 300 mL, operated under continuous gas flow, and was equipped with a condenser, kept at −15 °C at the outlet.[44] A broad-spectrum commercial (ACE-Hanovia) Hg lamp was used (Figure S1), which was immersed in the solution inside a water-cooled jacket that served as a UV cut-off filter (λ > 385 nm). The experiments were performed at atmospheric pressure and 20 °C. Before the photocatalytic test, the photocatalyst (300 mg) was dried at 100 °C, and $EtOH_{aq}$ (250 mL, 25% v/v) was purged with Ar; and the corresponding suspension was stirred in the reactor for 30 min under dark and N_2/Ar flow (99.999% N_2 was used as the internal standard) and then irradiated. No products were detected in the dark. After 10 min of light on, the evolved gaseous products were periodically analyzed online using a gas microchromatograph Varian CP-4900, equipped with micro-TCD detectors (detection limit for H_2, 50 ppm) and two columns (10 m PPQ, He carrier; 10 m molecular sieve (5 Å), Ar carrier).

After the test (4 h), the mixture was filtered, and the solution was analyzed by gas chromatography using Bruker 450 GC equipment with an FID detector and a CP-Sil 8 CB capillary column (30 m × 0.25 mm).

A reusability test was carried out with the most active photocatalyst; the used sample was removed from the liquid reaction mixture by filtering, washed with ethanol, and tested again. Moreover, in a separate cyclic experiment, the light was switched off after 1 h, and then after 0.5 h in dark conditions, the light was switched on for 1 h.

3. RESULTS AND DISCUSSION

3.1. Structural and Chemical Characterization. As stated in the Experimental Section, the $Mo_xCT/g\text{-}C_3N_4$ catalysts studied in this work were prepared by ultrasonic treatment of a suspension containing previously synthesized molybdenum carbide nanoparticles and $g\text{-}C_3N_4$ nanosheets. XRD patterns of the initial Mo_xC800 and Mo_xC900 (Figure S2) show the main presence of relatively narrow peaks that could be perfectly indexed with the hexagonal close-packed, hcp, $P6_3/mmc$, structure of Mo_2C (PDF 04-014-1517). The average crystallite size of Mo_2C was $\overline{d}$ = 22 and 30 nm in Mo_xC800 (from now Mo_2C800) and Mo_xC900 (from now Mo_2C900), respectively. On the other hand, in the XRD pattern of Mo_xC1100 (Figure S2), mainly 6 very wide peaks are observed that could be in principle be well indexed as the 111, 200, 220, 311, 222, and 400 reflections of the cubic close-packed, fcc, $Fm\bar{3}m$, the structure of MoC (PDF 04-003-1480) with $\overline{d}$ = 4 nm; for easy identification of this sample, from this point on it will be labeled MoC1100. Meanwhile, the XRD analysis of Mo_xC700 (Figure S2) shows both the presence of very wide peaks of the fcc structure of MoC and less wide peaks of the hcp structure of Mo_2C.

The XRD pattern of $g\text{-}C_3N_4$ prepared in this work shows a main peak at 2θ = 27.7° and a peak at 2θ = 13.0° with a much lower intensity (Figure 1). The peak at 2θ = 27.7° is due to 002 reflection of the (001) interlayer stacking; the position of

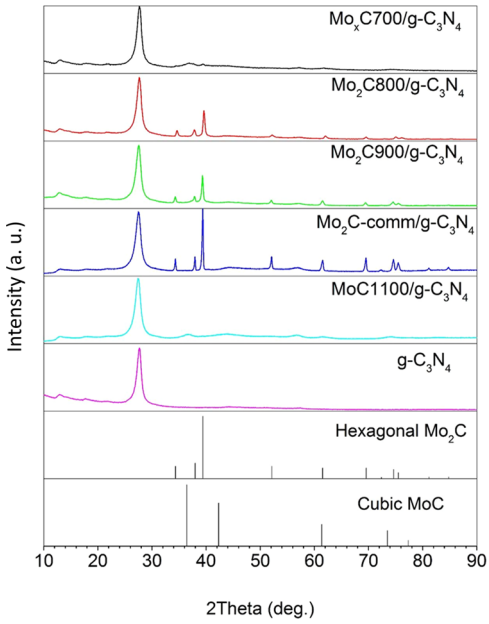

Figure 1. XRD patterns of nanocomposites and $g\text{-}C_3N_4$.

this peak indicates a slightly smaller interlayer distance with respect to bulk $g\text{-}C_3N_4$, which shows the 002 XRD peak at 27.34°.[40,45] The low intensity peak at 2θ = 13.0° is attributed to the in-plane structural packing motifs.[46]

The FTIR spectrum of $g\text{-}C_3N_4$ (Figure S3) agrees with that expected for this material.[40,45] The characteristic band of the breathing mode of s-triazine rings can be seen at 807 cm^{-1}; bands related to C═N and C−N stretchings in the heterocycles are visible in the 1800−900 cm^{-1} zone.[40,45] All of these FTIR features can also be seen in the spectra of all nanocomposites prepared (Figure S3).

All photocatalysts showed type IV N_2 adsorption−desorption isotherms with H3 hysteresis loops (Figure S4).[47] The S_{BET} values of 29−39 $m^2\ g^{-1}$ (Table 1), and wide pore size distributions in the range of meso- and macropores were found (Figure S5).

Figure 1 shows the XRD patterns of $Mo_xCT/g\text{-}C_3N_4$ nanocomposites. After the integration of Mo_xCT onto $g\text{-}C_3N_4$, the photocatalysts always retained the initial Mo_xC crystalline phases and $g\text{-}C_3N_4$ nanosheets used in their preparation (Figure 1).

For $Mo_2C900/g\text{-}C_3N_4$, $MoC1100/g\text{-}C_3N_4$, and $Mo_2Ccomm/g\text{-}C_3N_4$, the 002 interlayer-stacking peaks appeared at slightly a lower angle than that of the prepared $g\text{-}C_3N_4$ (2θ = 27.7°) (Table 1).

Table 1 shows the obtained crystallite sizes of the Mo_xC phases in the photocatalysts. The semiquantitative Mo_xC phase analysis of the $Mo_xC700/g\text{-}C_3N_4$ sample results in hcp Mo_2C (14%) and fcc MoC (86%).[43]

Hexagonal Mo_2C (11−31 nm crystallite size) was identified in the $Mo_xCT/g\text{-}C_3N_4$ (T = 700−900 °C) nanocomposites; the higher the temperature used in the preparation of Mo_xCT, the larger the Mo_2C crystallite size. $Mo_2C\text{-}comm/g\text{-}C_3N_4$ showed the largest hcp Mo_2C crystallite size (37 nm). On the other hand, the fcc MoC phase, which was determined in

https://doi.org/10.1021/acssuschemeng.3c06261
ACS Sustainable Chem. Eng. 2024, 12, 4365−4374

$Mo_xC700/g\text{-}C_3N_4$ and $MoC1100/g\text{-}C_3N_4$, showed a similar crystallite size (4 nm) in both nanocomposites.

Figure 2 displays TEM-HRTEM images of the $Mo_2C800/g\text{-}C_3N_4$, $Mo_2C900/g\text{-}C_3N_4$, and $MoC1100/g\text{-}C_3N_4$ photocatalysts; hcp Mo_2C nanoparticles were identified in $Mo_2C800/g\text{-}C_3N_4$ (mean size: 24.1 nm) and $Mo_2C900/g\text{-}C_3N_4$ (mean size: 30.2 nm), whereas cubic MoC nanoparticles were found in $MoC1100/g\text{-}C_3N_4$ (mean particle size: 5.1 nm). These findings agree with those determined by XRD analysis (Table 1).

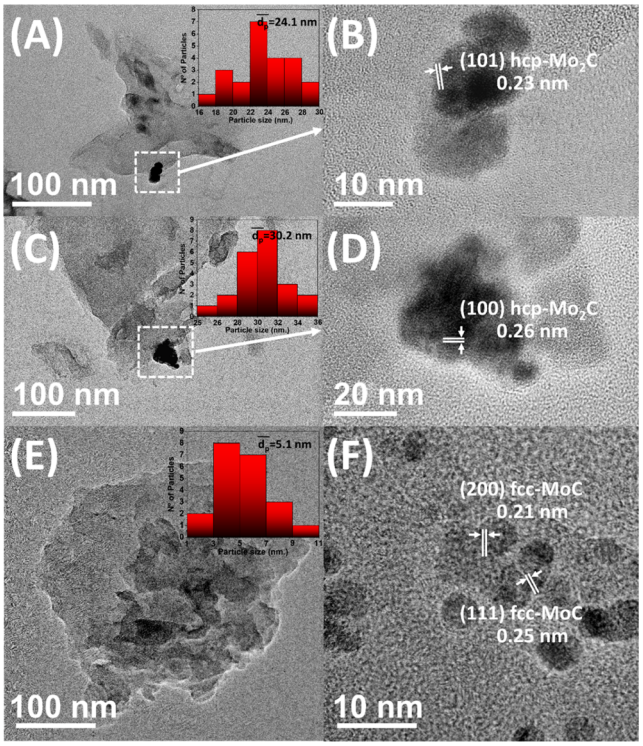

Figure 2. TEM-HRTEM images and particle distribution (insets) of (A) and (B) $Mo_2C800/g\text{-}C_3N_4$; (C) and (D) $Mo_2C900/g\text{-}C_3N_4$; and (E) and (F) $MoC1100/g\text{-}C_3N_4$ nanocomposites.

Figure 3 shows TEM and HRTEM images of $Mo_xC700/g\text{-}C_3N_4$. In this case, the nanoparticles of Mo_xC with two domains of particle size, with mean sizes of 4.3 and 13.0 nm, can be seen (Figure 3B). Moreover, the presence of hcp Mo_2C and fcc MoC in close proximity was determined by HRTEM (Figure 3C). These results are in good agreement with those of the XRD analysis. Moreover, EDX analysis showed that Mo was homogeneously distributed along the photocatalyst (Figure 3D).

The surface characteristics of the photocatalysts were analyzed by XPS. The XP C 1s spectrum corresponding to $g\text{-}C_3N_4$ (Figure S7) shows, besides the adventitious band due to C−C at 284.8 eV, a main band at about 288.1 eV, characteristic of bound C in the heterocycles (C−N═C).[40,48] In addition, a small C 1s component at a lower BE (283.3−283.8 eV), characteristic of carbides can be identified in the XP spectra of Mo_xC-containing photocatalysts (Figure S7).[24,37,38] In all cases, the broadness and asymmetry of the band located at the highest BE are indicative of the presence of O-bound (C−O, C═O) surface species.[24,40,49] The N 1s spectrum of $g\text{-}C_3N_4$ (Figure S7) shows a main component assigned to sp^2-bonded N in the heterocycles at about 398.6 eV, and components at higher BEs of 399.4, 401.0, and 404.7 eV. The signal at 399.4 eV can be attributed to the presence of tertiary nitrogen ($N\text{-}(C)_3$). On the other hand, amino functional groups (C−N−H), arising from a defective condensation of heptazine substructures, could be responsible for the component at 401.0 eV; the very low intense peak at 404.7 eV is attributed to the charging effects or positive charge localization in the heterocycles.[48,50,51] The N 1s spectra of the

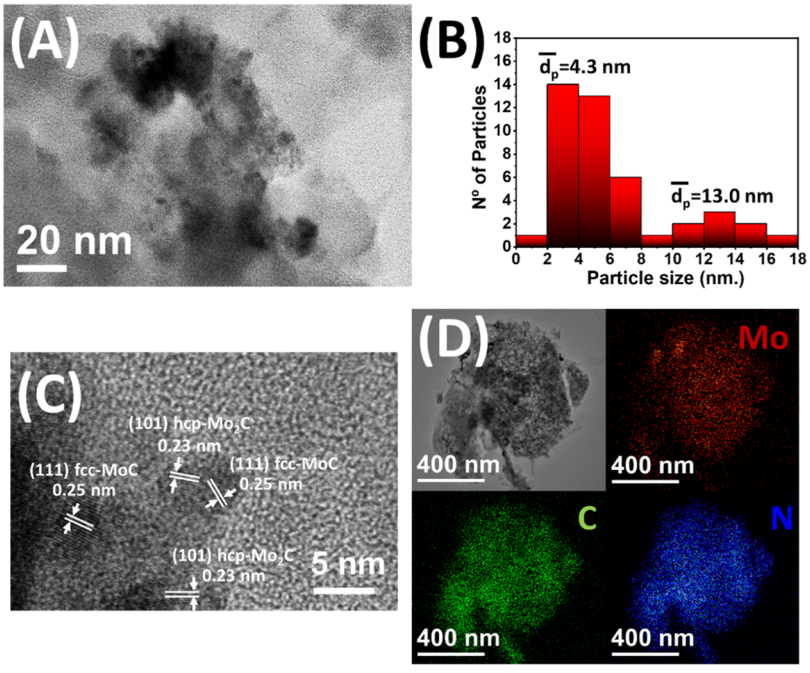

Figure 3. (A) TEM micrograph, (B) particle size distribution, (C) HRTEM micrograph, and (D) scanning transmission electron microscopy (STEM) image and EDX elemental mapping of the $Mo_xC700/g\text{-}C_3N_4$ photocatalyst.

https://doi.org/10.1021/acssuschemeng.3c06261
ACS Sustainable Chem. Eng. 2024, 12, 4365−4374

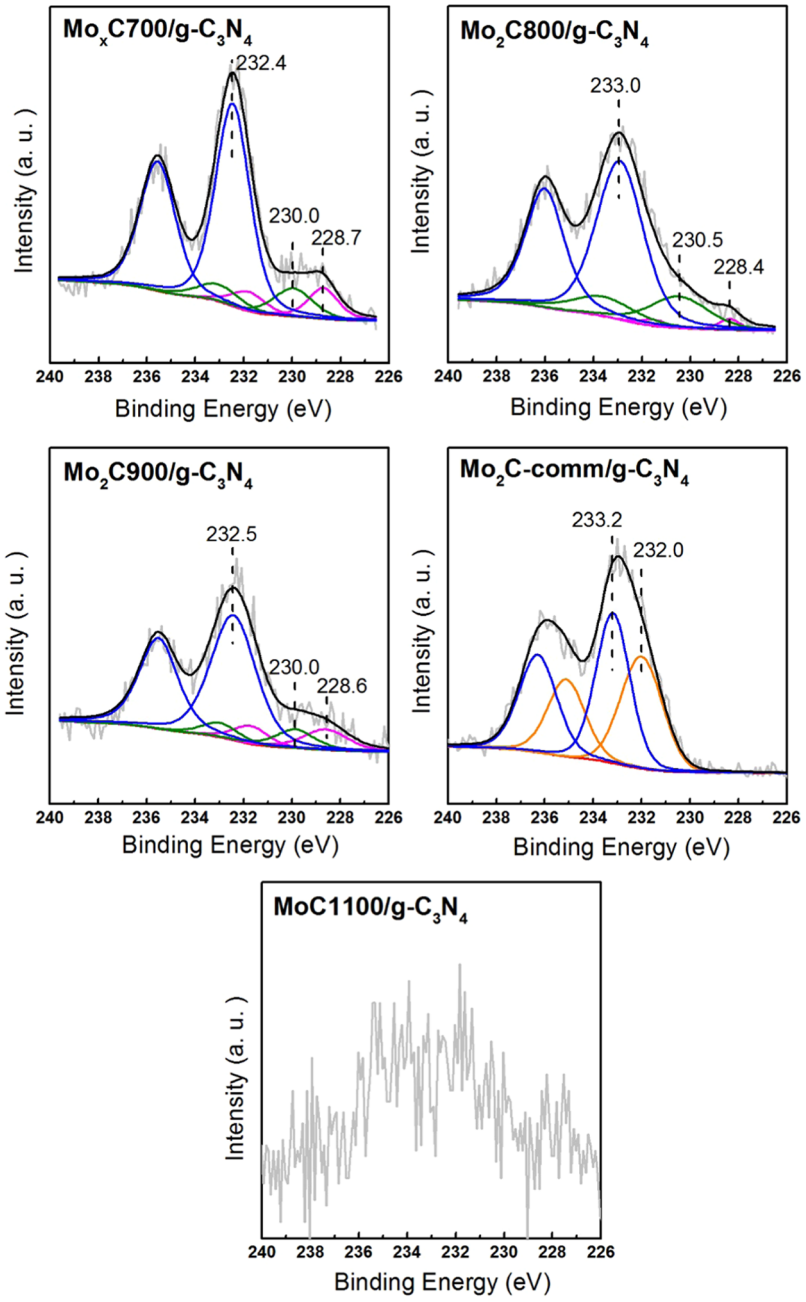

Figure 4. Mo 3d core level spectra of the nanocomposites.

nanocomposites were similar to those of g-C_3N_4 (Figure S7). On the other hand, the presence of a small amount of surface oxygen-containing species could be evidenced in all cases (Figure S8); the asymmetric broad O 1s band with a maximum at 532.6 eV in the XP spectrum of g-C_3N_4 could be assigned to adsorbed H_2O and surface species with C═O bonds.[40] Molybdenum oxide and/or oxycarbide species could contribute to the O 1s band in the XP spectra of Mo$_x$C-containing photocatalysts, whose maxima are located at a lower BE than that of g-C_3N_4.[24,49] Finally, Figure 4 shows the Mo 3d core level spectra of nanocomposites, which were deconvoluted fixing the Mo $3d_{5/2}$/Mo $3d_{3/2}$ intensity ratios of 1.5 and 3.1 eV as the value of orbital splitting.[52] The Mo $3d_{5/2}$ component at 228.4−228.7 eV indicates the presence of surface carbides and is attributed to Mo_2C and/or derived oxycarbide species.[24,37,49,53] The other Mo $3d_{5/2}$ components at higher BEs can be assigned to the Mo^{4+}, Mo^{5+}, and Mo^{6+} surface species, which could be related to MoC and/or different molybdenum oxycarbide and oxide species.[37,39,53] The samples Mo$_x$C700/g-C_3N_4, Mo$_x$C800/g-C_3N_4, and Mo$_x$C900/g-C_3N_4 showed clear Mo $3d_{5/2}$ components at a BE lower than 231 eV, and the corresponding molybdenum surface species were about 23% of the total Mo^{n+} surface species. Although the Mo 3d spectrum of MoC1100/g-C_3N_4 could not be properly deconvoluted, the existence of surface molybdenum carbide and oxide species could also be inferred in this case (Figure 4). In all cases, the contact of samples with ambient air could produce oxycarbide and oxide species.[24]

3.2. Photoelectrochemical Features and Photocatalytic Behavior. The optical properties of the photocatalysts were analyzed by UV−vis eliminate DRS and PL spectroscopy. Figure S9 shows the UV−vis DRS spectra and the

https://doi.org/10.1021/acssuschemeng.3c06261
ACS Sustainable Chem. Eng. 2024, 12, 4365−4374

corresponding Tauc plots used in the determination of the band gap values, following the approach reported in ref 54. In all cases, light absorption edges occurred in the visible region (Table 1). The band gap determined for g-C_3N_4 is 2.75 eV, and all of the Mo_xCT/g-C_3N_4 nanocomposites showed only slightly higher band gap values (2.77−2.79 eV).

The recombination process of photogenerated (e^-/h^+) pairs in the photocatalysts was studied by PL analysis. Figure 5

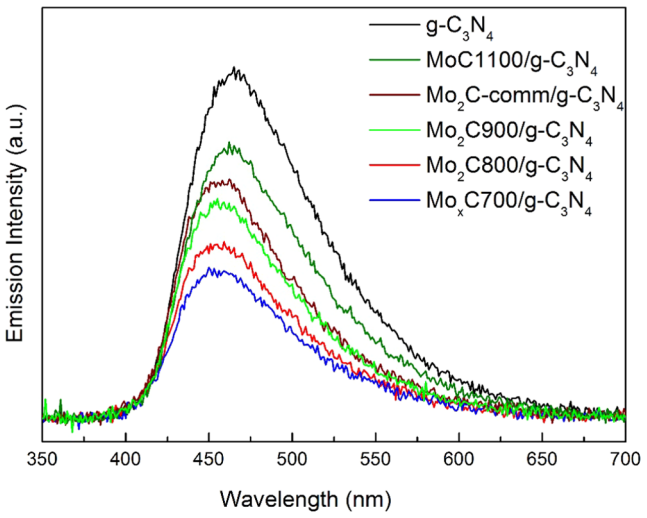

Figure 5. Photoluminescence spectra of nanocomposites and g-C_3N_4.

shows the PL spectra of the nanocomposites compared to that of g-C_3N_4. We observed an emission peak in the visible region for all samples, a maximum at 465 nm for g-C_3N_4, and a slight shift of the emission maxima toward higher energies for the Mo_xC-containing photocatalysts. These findings are consistent with the UV−vis DRS results, which indicate a slight increase in the band gap energy for Mo_xCT/g-C_3N_4 than pristine g-C_3N_4. Interestingly, the intensity of the PL spectrum of g-C_3N_4 is always higher than that of nanocomposites (Figure 5), indicating that the presence of Mo_xC decreases the e^-/h^+ pair recombination rate, thus leading to a decrease in the emission intensity. The trend in the intensity of the PL emission band (Figure 5) suggests that hcp Mo_2C is more effective in reducing charge recombination in g-C_3N_4 than fcc MoC. Moreover, it seems that recombination is less favored when the Mo_2C crystallite size decreases and when hcp Mo_2C and fcc MoC are in close proximity over g-C_3N_4. A low recombination rate of the photogenerated (e^-/h^+) pairs and a faster electron transfer rate can improve the photocatalytic properties.

To further evaluate the photocharge separation and electron transfer properties of the photocatalysts, electrochemical impedance spectra, and transient photocurrent response were measured, as described in the Experimental Section.

Figure 6 shows the impedance Nyquist plots for the g-C_3N_4 and Mo_xCT/g-C_3N_4 photocatalysts under dark (A) and illumination (B) conditions. As can be seen, in both cases, g-C_3N_4 shows a larger arc radius than the Mo_xC-containing nanocomposites, indicating that the presence of Mo_xC on the g-C_3N_4 nanosheets reduces the electron transfer resistance in the dark and under irradiation. Moreover, in all cases, the arc radius in the dark is larger than that under irradiation, as illustrated in Figure S10 for the samples with the largest and the smallest arc radii, g-C_3N_4 and Mo_xC700/g-C_3N_4, respectively. This indicates the effectiveness of irradiation in

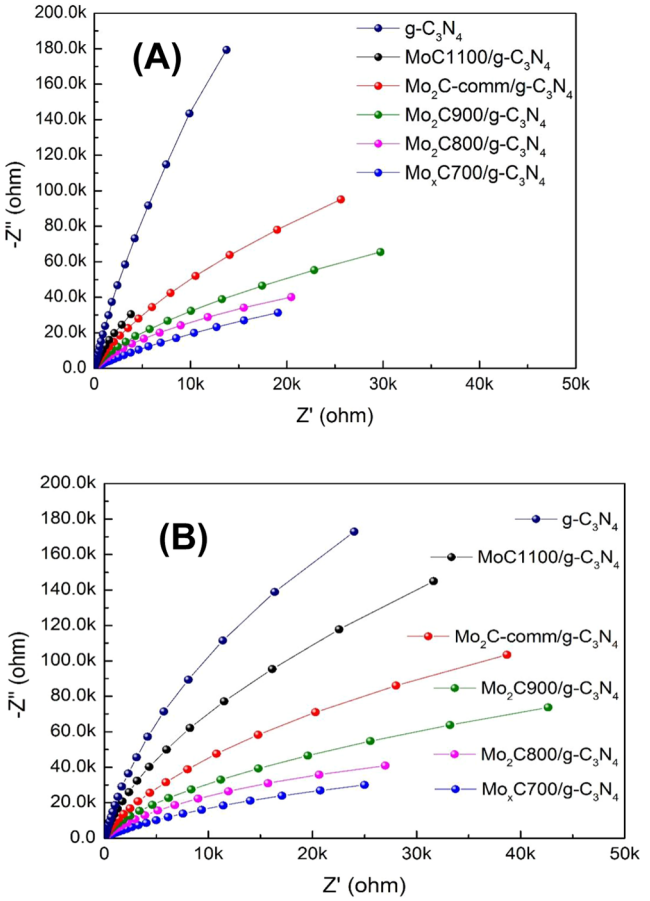

Figure 6. EIS Nyquist plots of nanocomposites and g-C_3N_4: (A) under dark conditions and (B) with irradiation.

decreasing the barrier of electron transfer in these materials. The Nyquist arc radius follows a trend similar to that of the intensity of the PL spectra shown above; the lower the electron transfer barrier, the higher the efficiency of charge separation.

The results of the transient photocurrent responses are shown in Figure 7. The Mo_xC-containing nanocomposites

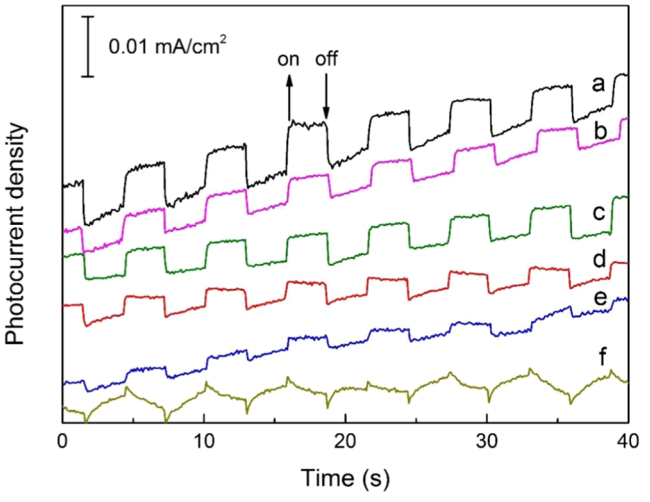

Figure 7. Transient photocurrent responses of nanocomposites and g-C_3N_4: (a) Mo_xC700/g-C_3N_4; (b) Mo_2C800/g-C_3N_4; (c) Mo_2C900/g-C_3N_4; (d) Mo_2C-comm/g-C_3N_4; (e) MoC1100/g-C_3N_4; and (f) g-C_3N_4.

https://doi.org/10.1021/acssuschemeng.3c06261
ACS Sustainable Chem. Eng. 2024, 12, 4365−4374

showed a larger photocurrent density than that of g-C_3N_4. $Mo_xC700/g\text{-}C_3N_4$ showed the highest photocurrent density. The presence of Mo_xC as a cocatalyst slows down the recombination rate of photogenerated e^-/h^+, decreases the barrier for electron transport, and accordingly can favor the further transfer of electrons for proton reduction.

As stated above, the photocatalytic behavior in H_2 generation from $EtOH_{aq}$ (25% v/v) was analyzed under visible light (λ > 385 nm) for all of the materials prepared, including pristine g-C_3N_4, and a blank test without the photocatalyst was also carried out. Under the experimental conditions used in this work, g-C_3N_4 and the blank test produced a negligible amount of H_2. On the other hand, all nanocomposites containing molybdenum carbide species were active in photocatalytic H_2 generation; the H_2 production per gram of catalyst over time is depicted in Figure 8. Besides H_2, minor

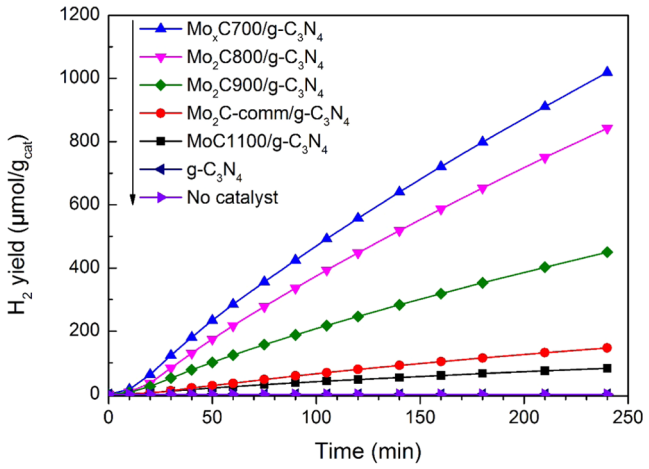

Figure 8. H_2 generated per gram of photocatalyst as a function of irradiation time; results from g-C_3N_4 and the blank test are also included. Reaction conditions: 25% v/v ethanol aqueous solution and T = 20 °C.

amounts of CO_2 were produced; moreover, mainly 2,3-butanediol was found in the liquid phase, and no O_2 was detected. These results point out that photoreforming of ethanol was not accomplished. Moreover, the absence of CH_4 and CO as products in the gas phase suggests that under our experimental conditions and with$Mo_xC/g\text{-}C_3N_4$ photocatalysts, the cleavage of the C−C bond is not favored in the ethanol phototransformation.[1,2,4] The oxidation of ethanol could proceed with the generated hole (h^+), and the α-hydroxyethyl radicals ($^\bullet CH(OH)CH_3$) be formed:[38,55,56]

$$CH_3CH_2OH + h^+ \rightarrow {}^\bullet CH(OH)CH_3 + H^+ \quad (1)$$

Then, the coupling of two initially formed α-hydroxyethyl radicals ($^\bullet CH(OH)CH_3$) could be proposed for the formation of 2,3-butanediol:[38,44,56,57]

$$2{}^\bullet CH(OH)CH_3 \rightarrow CH_3CH(OH)CH(OH)CH_3 \quad (2)$$

According to the characterization results given above, the molybdenum carbide species on g-C_3N_4 mainly facilitate electronic transfer, producing H_2 and decreasing e^-/h^+ recombination in g-C_3N_4. This is illustrated in Figure S11 for $Mo_xC700/g\text{-}C_3N_4$.

Figure 8 shows the hydrogen production per gram of the $Mo_xCT/g\text{-}C_3N_4$ photocatalyst; a similar trend is found when H_2 production is referred to as a gram of Mo (Figure S12). The photocatalytic performance can be straightforwardly related to the photoelectrochemical characteristics of the samples: the intensity of the PL emission peak, EIS values, and transient photocurrent measurements. The smaller the size of the hcp Mo_2C particles in the nanocomposite, the better the photocatalytic performance. Moreover, a positive effect of the close proximity of the hcp Mo_2C and fcc MoC phases is found. $Mo_xC700/g\text{-}C_3N_4$ with both hcp Mo_2C (11 nm) and fcc MoC (4 nm) showed the best photocatalytic behavior. The presence of heterojunctions MoC-Mo_2C could improve the photocatalytic behavior, as has been demonstrated for WC-Mo_2C/TiO_2 photocatalysts with WC-Mo_2C heterojunctions.[58] In fact, as stated in the Introduction section, for Mo_xC-based electrocatalysts, the presence of MoC/Mo_2C heterostructures was demonstrated to improve the H_2 evolution reaction,[36] and an improved photocatalytic behavior for H_2 production could be expected,[35] which is in line with the results presented here.

In order to know the reusability of the most performant photocatalyst, a new photocatalytic test was carried out with the used $Mo_xC700/g\text{-}C_3N_4$ (Figure 9), and a similar H_2

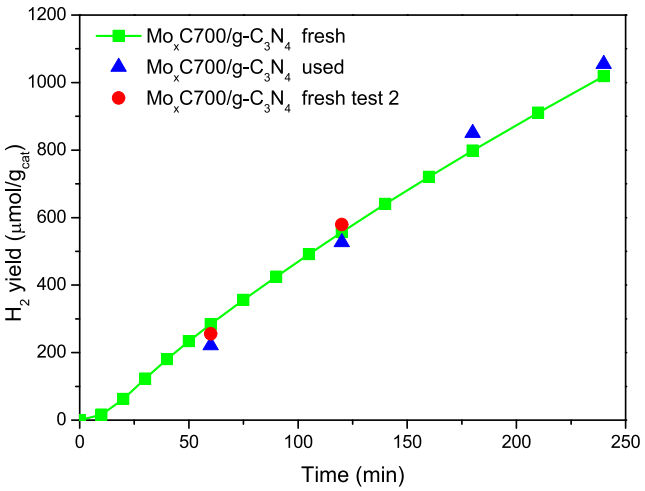

Figure 9. Different photocatalytic tests for H_2 production over fresh and used $Mo_xC700/g\text{-}C_3N_4$. In test 2, the light was switched off after 1 h; then, after 0.5 h in dark conditions, the light was switched on. Reaction conditions: 25% v/v ethanol aqueous solution and T = 20 °C.

production for both fresh and used catalysts was observed. Figure 9 also shows the reproducibility of the photocatalytic behavior of fresh $Mo_xC700/g\text{-}C_3N_4$ when the light switch off/switch on procedure was employed. In all cases, the standard deviation was only up to 2% of the values originally obtained. The reused $Mo_xC700/g\text{-}C_3N_4$ was characterized by FTIR and XRD, and similar results were obtained for the fresh photocatalysts (Figures S13 and S14). These results show the stability of $Mo_xC700/g\text{-}C_3N_4$, which can be reused without loss of its properties.

4. CONCLUSIONS

The preparation method led to tailored $Mo_xCT/g\text{-}C_3N_4$ photocatalysts with hcp Mo_2C and/or fcc MoC nanoparticles of different sizes supported on g-C_3N_4 nanosheets. The separately prepared Mo_xC cocatalysts were incorporated into g-C_3N_4 using ultrasound, which maintained the characteristics

https://doi.org/10.1021/acssuschemeng.3c06261
ACS Sustainable Chem. Eng. 2024, 12, 4365−4374

of both Mo_xC nanoparticles and g-C_3N_4 nanosheets formerly synthesized.

The photocatalytic behavior of Mo_xCT/g-C_3N_4 in hydrogen generation from $EtOH_{aq}$ under visible light is related to the rate of recombination of photogenerated charges, electron transfer resistance, and photocurrent response of the prepared nanocomposites. These properties depend on the characteristics of the Mo_xC cocatalyst. Photocatalysts containing hcp Mo_2C were more effective than that containing only fcc MoC; the smaller the crystallite size of hcp Mo_2C, the better was the photocatalytic performance of Mo_xCT/g-C_3N_4. The best photocatalytic results were obtained for Mo_xC700/g-C_3N_4, which presented hexagonal Mo_2C and cubic MoC, the lowest rate of charge recombination and electron transfer resistance, and the highest photocurrent response; about 7 mmol of H_2 g_{Mo}^{-1} h^{-1} were produced with this photocatalyst under the conditions used. The improved photocatalytic behavior of Mo_xC700/g-C_3N_4 could be related to the presence of MoC-Mo_2C heterojunctions, which could enhance the photoelectrochemical properties of the nanocomposites and therefore photocatalytic H_2 generation. Moreover, the reusability of Mo_xC700/g-C_3N_4 is demonstrated.

■ ASSOCIATED CONTENT

Supporting Information

The Supporting Information is available free of charge at https://pubs.acs.org/doi/10.1021/acssuschemeng.3c06261.

Additional details related to characterization methods and characterization and photocatalytic results are included (PDF)

■ AUTHOR INFORMATION

Corresponding Author

Narcís Homs − *Departament de Química Inorgànica i Orgànica, secció de Química Inorgànica & Institut de Nanociència i Nanotecnologia (IN2UB), Universitat de Barcelona, 08028 Barcelona, Spain; Catalonia Institute for Energy Research (IREC), 08930 Barcelona, Spain;* orcid.org/0000-0002-0847-7327; Email: narcis.homs@qi.ub.edu

Authors

Yan Wang − *Departament de Química Inorgànica i Orgànica, secció de Química Inorgànica & Institut de Nanociència i Nanotecnologia (IN2UB), Universitat de Barcelona, 08028 Barcelona, Spain; Catalonia Institute for Energy Research (IREC), 08930 Barcelona, Spain;* Present Address: Shenzhen Institute of Advanced Technology, Chinese Academy of Sciences, 1068 Xueyuan Avenue, Shenzhen University Town, 518071 Shenzhen, China

Arturo Pajares − *Departament de Química Inorgànica i Orgànica, secció de Química Inorgànica & Institut de Nanociència i Nanotecnologia (IN2UB), Universitat de Barcelona, 08028 Barcelona, Spain; Catalonia Institute for Energy Research (IREC), 08930 Barcelona, Spain;* Present Address: Sustainable Materials Management, Flemish Institute for Technological Research (VITO NV), Boeretang 200, 2400 Mol, Belgium.; orcid.org/0000-0002-0160-2770

Jarosław Serafin − *Departament de Química Inorgànica i Orgànica, secció de Química Inorgànica & Institut de Nanociència i Nanotecnologia (IN2UB), Universitat de Barcelona, 08028 Barcelona, Spain*

Xavier Alcobé − *Unitat de Difracció de Raigs X, Centres Científics i Tecnològics (CCiTUB), Universitat de Barcelona, 08028 Barcelona, Spain*

Frank Güell − *ENPHOCAMAT Group, Institut de Nanociència i Nanotecnologia (IN2UB), Universitat de Barcelona, 08028 Barcelona, Spain*

Pilar Ramírez de la Piscina − *Departament de Química Inorgànica i Orgànica, secció de Química Inorgànica & Institut de Nanociència i Nanotecnologia (IN2UB), Universitat de Barcelona, 08028 Barcelona, Spain*

Complete contact information is available at: https://pubs.acs.org/10.1021/acssuschemeng.3c06261

Notes

The authors declare no competing financial interest.

■ ACKNOWLEDGMENTS

The authors acknowledge the financial support of the MICINN MAT2017-87500-P and PID2020-116031RB-I00/AEI/10.13039/501100011033/FEDER projects and CCiTUB for technical facilities. Y.W. and A.P. acknowledge the predoctoral grants from the China Scholarship Council (CSC 201608460014) and MINECO (BES-C-2015-074574), Spain, respectively.

■ REFERENCES

(1) Beltram, A.; Melchionna, M.; Montini, T.; Nasi, L.; Fornasiero, P.; Prato, M. Making H_2 from light and biomass-derived alcohols: the outstanding activity of newly designed hierarchical MWCNT/Pd@TiO_2 hybrid catalysts. *Green Chem.* **2017**, *19* (10), 2379−2389.

(2) Zhang, X.; Luo, L.; Yun, R.; Pu, M.; Zhang, B.; Xiang, X. Increasing the Activity and Selectivity of TiO_2-Supported Au Catalysts for Renewable Hydrogen Generation from Ethanol Photoreforming by Engineering Ti^{3+} Defects. *ACS Sustainable Chem. Eng.* **2019**, *7* (16), 13856−13864.

(3) Chen, W. T.; Dong, Y.; Yadav, P.; Aughterson, R. D.; Sun-Waterhouse, D.; Waterhouse, G. I. Effect of alcohol sacrificial agent on the performance of Cu/TiO_2 photocatalysts for UV-driven hydrogen production. *Appl. Catal., A* **2020**, *602*, No. 117703.

(4) Karimi Estahbanati, M.; Babin, A.; Feilizadeh, M.; Nayernia, Z.; Mahinpey, N.; Iliuta, M. C. Photocatalytic conversion of alcohols to hydrogen and carbon-containing products: A cleaner alcohol valorization approach. *J. Cleaner Prod.* **2021**, *318*, No. 128546.

(5) Wang, X.; Blechert, S.; Antonietti, M. Polymeric graphitic carbon nitride for heterogeneous photocatalysis. *ACS Catal.* **2012**, *2* (8), 1596−1606.

(6) Cao, S.; Low, J.; Yu, J.; Jaroniec, M. Polymeric photocatalysts based on graphitic carbon nitride. *Adv. Mater.* **2015**, *27* (13), 2150−2176.

(7) Jiang, L.; Yuan, X.; Pan, Y.; Liang, J.; Zeng, G.; Wu, Z.; Wang, H. Doping of graphitic carbon nitride for photocatalysis: A review. *Appl. Catal., B* **2017**, *217* (15), 388−406.

(8) Nasir, M. S.; Yang, G.; Ayub, I.; Wang, S.; Wang, L.; Wang, X.; Yan, W.; Peng, S.; Ramakarishna, S. Recent development in graphitic carbon nitride based photocatalysis for hydrogen generation. *Appl. Catal., B* **2019**, *257* (15), No. 117855.

(9) Wang, L.; Wang, K.; He, T.; Zhao, Y.; Song, H.; Wang, H. Graphitic Carbon Nitride-Based Photocatalytic Materials: Preparation Strategy and Application. *ACS Sustainable Chem. Eng.* **2020**, *8* (43), 16048−16085.

(10) Liu, E.; Lin, X.; Hong, Y.; Yang, L.; Luo, B.; Shi, W.; Shi, J. Rational copolymerization strategy engineered C self-doped g-C_3N_4 for efficient and robust solar photocatalytic H_2 evolution. *Renewable Energy* **2021**, *178*, 757−765.

(11) Ma, D.; Zhang, Z.; Zou, Y.; Chen, J.; Shi, J. The progress of g-C_3N_4 in photocatalytic H_2 evolution: From fabrication to modification. *Coord. Chem. Rev.* **2024**, *500*, No. 215489.
(12) Zhang, P.; Wang, T.; Chang, X.; Gong, J. Effective charge carrier utilization in photocatalytic conversions. *Acc. Chem. Res.* **2016**, *49* (5), 911−921.
(13) Ran, J.; Zhang, J.; Yu, J.; Jaroniec, M.; Qiao, S. Z. Earth-abundant cocatalysts for semiconductor-based photocatalytic water splitting. *Chem. Soc. Rev.* **2014**, *43* (22), 7787−7812.
(14) Zhou, Y.; Wang, W.; Zhang, C.; Huang, D.; Lai, C.; Cheng, M.; Qin, L.; Yang, Y.; Zhou, C.; Li, B.; Luo, H.; He, D. Sustainable hydrogen production by molybdenum carbide based efficient photocatalysts: From properties to mechanism. *Adv. Colloid Interface Sci.* **2020**, *279*, No. 102144.
(15) *The Chemistry of Transition Metal Carbides and Nitrides*; Oyama, S. T., Ed.; Blackie Academic and Professional: London, 1996.
(16) Hwu, H. H.; Chen, J. G. Surface chemistry of transition metal carbides. *Chem. Rev.* **2005**, *105* (1), 185−212.
(17) Prats, H.; Piñero, J. J.; Viñes, F.; Bromley, S. T.; Sayós, R.; Illas, F. Assessing the usefulness of transition metal carbides for hydrogenation reactions. *Chem. Commun.* **2019**, *55* (85), 12797−12800.
(18) Figueras, M.; Gutiérrez, R. A.; Viñes, F.; Ramírez, P. J.; Rodriguez, J. A.; Illas, F. Supported molybdenum carbide nanoparticles as hot hydrogen reservoirs for catalytic applications. *J. Phys. Chem. Lett.* **2020**, *11* (19), 8437−8441.
(19) Pajares, A.; Wang, Y.; Kronenberg, M. J.; de la Piscina, P. R.; Homs, N. Photocatalytic H_2 production from ethanol aqueous solution using TiO_2 with tungsten carbide nanoparticles as co-catalyst. *Int. J. Hydrogen Energy* **2020**, *45* (40), 20558−20567.
(20) Chen, W. F.; Wang, C. H.; Sasaki, K.; Marinkovic, N.; Xu, W.; Muckerman, J. T.; Zhu, Y.; Adzic, R. R. Highly active and durable nanostructured molybdenum carbide electrocatalysts for hydrogen production. *Energy Environ. Sci.* **2013**, *6* (3), 943−951.
(21) Wang, S.; Wang, J.; Zhu, M.; Bao, X.; Xiao, B.; Su, D.; Li, H.; Wang, Y. Molybdenum-carbide-modified nitrogen-doped carbon vesicle encapsulating nickel nanoparticles: a highly efficient, low-cost catalyst for hydrogen evolution reaction. *J. Am. Chem. Soc.* **2015**, *137* (50), 15753−15759.
(22) Xiao, T. C.; York, A. P.; Williams, V. C.; Al-Megren, H.; Hanif, A.; Zhou, X. Y.; Green, M. L. Preparation of molybdenum carbides using butane and their catalytic performance. *Chem. Mater.* **2000**, *12* (2), 3896−3905.
(23) Liu, W.; Chen, B.; Duan, X.; Wu, K. H.; Qi, W.; Guo, X.; Zhang, B.; Su, D. Molybdenum carbide modified nanocarbon catalysts for alkane dehydrogenation reactions. *ACS Catal.* **2017**, *7* (9), 5820−5827.
(24) Liu, X.; Kunkel, C.; Ramirez de la Piscina, P.; Homs, N.; Vines, F.; Illas, F. Effective and highly selective CO generation from CO_2 using a polycrystalline α-Mo_2C catalyst. *ACS Catal.* **2017**, *7* (7), 4323−4335.
(25) Patterson, P. M.; Das, T. K.; Davis, B. H. Carbon monoxide hydrogenation over molybdenum and tungsten carbides. *Appl. Catal., A* **2003**, *251* (2), 449−455.
(26) Zhang, Y.; Wang, Y.; Guo, C.; Wang, Y. Molybdenum carbide-based photocatalysts: synthesis, functionalization, and applications. *Langmuir* **2022**, *38* (42), 12739−12756.
(27) Yue, X.; Yi, S.; Wang, R.; Zhang, Z.; Qiu, S. A novel architecture of dandelion-like Mo_2C/TiO_2 heterojunction photocatalysts towards high-performance photocatalytic hydrogen production from water splitting. *J. Mater. Chem. A* **2017**, *5* (21), 10591−10598.
(28) Ma, B.; Xu, H.; Lin, K.; Li, J.; Zhan, H.; Liu, W.; Li, C. Mo_2C as Non-Noble metal Co-catalyst in Mo_2C/CdS composite for enhanced photocatalytic H_2 evolution under visible light irradiation. *ChemSusChem* **2016**, *9* (8), 820−824.
(29) Yi, S. S.; Yan, J. M.; Wulan, B. R.; Jiang, Q. Efficient visible-light-driven hydrogen generation from water splitting catalyzed by highly stable CdS@Mo_2C−C core−shell nanorods. *J. Mater. Chem. A* **2017**, *5* (30), 15862−15868.
(30) Yue, X.; Yi, S.; Wang, R.; Zhang, Z.; Qiu, S. Well-controlled $SrTiO_3$@Mo_2C core-shell nanofiber photocatalyst: Boosted photogenerated charge carriers transportation and enhanced catalytic performance for water reduction. *Nano Energy* **2018**, *47*, 463−473.
(31) Dong, J.; Shi, Y.; Huang, C.; Wu, Q.; Zeng, T.; Yao, W. A new and stable Mo-Mo_2C modified g-C_3N_4 photocatalyst for efficient visible light photocatalytic H_2 production. *Appl. Catal., B* **2019**, *243*, 27−35.
(32) Zou, Y.; Ma, D.; Sun, D.; Mao, S.; He, C.; Wang, Z. X.; Ji, X.; Shi, J.-W. Carbon nanosheet facilitated charge separation and transfer between molybdenum carbide and graphitic carbon nitride toward efficient photocatalytic H_2 production. *Appl. Surf. Sci.* **2019**, *473*, 91−101.
(33) Song, Y.; Xia, K.; Gong, Y.; Chen, H.; Li, L.; Yi, J.; She, X.; Chen, Z.; Wu, J.; Li, H.; Xu, H. Controllable synthesized heterostructure photocatalyst Mo_2C@C/2D g-C_3N_4: enhanced catalytic performance for hydrogen production. *Dalton Trans.* **2018**, *47* (41), 14706−14712.
(34) Zhang, J.; Wu, M.; He, B.; Wang, R.; Wang, H.; Gong, Y. Facile synthesis of rod-like g-C_3N_4 by decorating Mo_2C co-catalyst for enhanced visible-light photocatalytic activity. *Appl. Surf. Sci.* **2019**, *470*, 565−572.
(35) Zheng, Y.; Dong, J.; Huang, C.; Xia, L.; Wu, Q.; Xu, Q.; Yao, W. Co-doped Mo-Mo_2C cocatalyst for enhanced g-C_3N_4 photocatalytic H_2 evolution. *Appl. Catal., B* **2020**, *260*, No. 118220.
(36) Zhang, X.; Wang, J.; Guo, T.; Liu, T.; Wu, Z.; Cavallo, L.; Cao, Z.; Wang, D. Z. Structure and phase regulation in Mo_xC (α-MoC_{1-x}/β-Mo_2C) to enhance hydrogen evolution. *Appl. Catal., B* **2019**, *247*, 78−85.
(37) Liu, X.; Pajares, A.; Matienzo, D. D. C.; Ramírez de la Piscina, P.; Homs, N. Preparation and characterization of bulk Mo_xC catalysts and their use in the reverse water-gas shift reaction. *Catal. Today* **2020**, *356* (1), 384−389.
(38) Wang, Y.; Mino, L.; Pellegrino, F.; Homs, N.; Ramírez de la Piscina, P. Engineered Mo_xC/TiO_2 interfaces for efficient noble metal-free photocatalytic hydrogen production. *Appl. Catal., B* **2022**, *318* (5), No. 121783.
(39) Pajares, A.; Liu, X.; Busacker, J. R.; Ramírez de la Piscina, P.; Homs, N. Supported Nanostructured Mo_xC Materials for the Catalytic Reduction of CO_2 through the Reverse Water Gas Shift Reaction. *Nanomaterials* **2022**, *12* (18), 3165−3180.
(40) She, X.; Wu, J.; Zhong, J.; Xu, H.; Yang, Y.; Vajtai, R.; Lou, J.; Liu, Y.; Du, D.; Li, H.; Ajayan, P. M. Oxygenated monolayer carbon nitride for excellent photocatalytic hydrogen evolution and external quantum efficiency. *Nano Energy* **2016**, *27*, 138−146.
(41) Gates-Rector, S.; Blanton, T. The powder diffraction file: A quality materials characterization database. *Powder Diffr.* **2019**, *34* (4), 352−360.
(42) Scherrer, P. Bestimmung der Grösse und der inneren Struktur von Kolloiteilchen mitels Röntgenstrahlen. *Nachr. Ges. Wiss. Goettingen, Math.-Phys. Kl.* **1918**, *2*, 98−100.
(43) Snyder, R. L. The use of reference intensity ratios in X-Ray quantitative analysis. *Powder Diffr.* **1992**, *7*, 186−193.
(44) Sola, A. C.; Ramírez de la Piscina, P.; Homs, N. Behaviour of Pt/TiO_2 catalysts with different morphological and structural characteristics in the photocatalytic conversion of ethanol aqueous solutions. *Catal. Today* **2020**, *341* (1), 13−20.
(45) Niu, P.; Zhang, L.; Liu, G.; Cheng, H. M. Graphene-like carbon nitride nanosheets for improved photocatalytic activities. *Adv. Funct. Mater.* **2012**, *22* (22), 4763−4770.
(46) Hu, C.; Hung, W. Z.; Wang, M. S.; Lu, P. J. Phosphorous and sulfur codoped g-C_3N_4 as an efficient metal-free photocatalyst. *Carbon* **2018**, *127*, 374−383.
(47) Thommes, M.; Kaneko, K.; Neimark, A. V.; Olivier, J. P.; Rodriguez-Reinoso, F.; Rouquerol, J.; Sing, K. S. Physisorption of gases, with special reference to the evaluation of surface area and pore

https://doi.org/10.1021/acssuschemeng.3c06261
ACS Sustainable Chem. Eng. 2024, 12, 4365−4374

size distribution (IUPAC Technical Report). *Pure Appl. Chem.* **2015**, *87* (9−10), 1051−1069.
(48) Gu, Q.; Liao, Y.; Yin, L.; Long, J.; Wang, X.; Xue, C. Template-free synthesis of porous graphitic carbon nitride microspheres for enhanced photocatalytic hydrogen generation with high stability. *Appl. Catal., B* **2015**, *165*, 503−510.
(49) Gao, Q.; Zhao, X.; Xiao, Y.; Zhao, D.; Cao, M. A mild route to mesoporous Mo_2C−C hybrid nanospheres for high performance lithium-ion batteries. *Nanoscale* **2014**, *6* (11), 6151−6157.
(50) Jiang, Y.; Sun, Z.; Tang, C.; Zhou, Y.; Zeng, L.; Huang, L. Enhancement of photocatalytic hydrogen evolution activity of porous oxygen doped g-C_3N_4 with nitrogen defects induced by changing electron transition. *Appl. Catal., B* **2019**, *240*, 30−38.
(51) Long, B.; Lin, J.; Wang, X. Thermally-induced desulfurization and conversion of guanidine thiocyanate into graphitic carbon nitride catalysts for hydrogen photosynthesis. *J. Mater. Chem. A* **2014**, *2* (9), 2942−2951.
(52) Oshikawa, K.; Nagai, M.; Omi, S. Characterization of molybdenum carbides for methane reforming by TPR, XRD, and XPS. *J. Phys. Chem. B* **2001**, *105* (38), 9124−9131.
(53) Porosoff, M. D.; Yang, X.; Boscoboinik, J. A.; Chen, J. G. Molybdenum carbide as alternative catalysts to precious metals for highly selective reduction of CO_2 to CO. *Angew. Chem.* **2014**, *126* (26), 6823−6827.
(54) Makuła, P.; Pacia, M.; Macyk, W. How To Correctly Determine the Band Gap Energy of Modified Semiconductor Photocatalysts Based on UV-Vis Spectra. *J. Phys. Chem. Lett.* **2018**, *9* (23), 6814−6817.
(55) Wang, J.; Yang, P.; Cao, B.; Zhao, J.; Zhu, Z. Photocatalytic carbon−carbon bond formation with concurrent hydrogen evolution on the Pt/TiO2 nanotube. *Appl. Surf. Sci.* **2015**, *325*, 86−90.
(56) Sola, A. C.; Homs, N.; Ramírez de la Piscina, P. Photocatalytic H2 production from ethanol(aq) solutions: The effect of intermediate products. *Int. J. Hydrogen Energy* **2016**, *41* (43), 19629−19636.
(57) Lu, H.; Zhao, J.; Li, L.; Gong, L.; Zheng, J.; Zhang, L.; Wang, Z.; Zhang, J.; Zhu, Z. Selective oxidation of sacrificial ethanol over TiO2-based photocatalysts during water splitting. *Energy Environ. Sci.* **2011**, *4* (9), 3384−3388.
(58) Gao, L.; Liu, J.; Long, H.; Wang, P.; Yu, H. One-step calcination synthesis of WC-Mo_2C heterojunction nanoparticles as novel H_2-production cocatalysts for enhanced photocatalytic activity of TiO_2. *Catal. Sci. Technol.* **2021**, *11* (22), 7307−7315.

https://doi.org/10.1021/acssuschemeng.3c06261
ACS Sustainable Chem. Eng. 2024, 12, 4365−4374